PHYSICAL REVIEW E **85**, 026319 (2012)

Splash control of drop impacts with geometric targets

Gabriel Juarez, Thomai Gastopoulos, Yibin Zhang, Michael L. Siegel, and Paulo E. Arratia[*]

Department of Mechanical Engineering and Applied Mechanics, University of Pennsylvania, Philadelphia, Pennsylvania 19104, USA

(Received 11 November 2011; revised manuscript received 19 January 2012; published 28 February 2012)

Drop impacts on solid and liquid surfaces exhibit complex dynamics due to the competition of inertial, viscous, and capillary forces. After impact, a liquid lamella develops and expands radially, and under certain conditions, the outer rim breaks up into an irregular arrangement of filaments and secondary droplets. We show experimentally that the lamella expansion and subsequent breakup of the outer rim can be controlled by length scales that are of comparable dimension to the impacting drop diameter. Under identical impact parameters (i.e., fluid properties and impact velocity) we observe unique splashing dynamics by varying the target cross-sectional geometry. These behaviors include (i) geometrically shaped lamellae and (ii) a transition in splashing stability, from regular to irregular splashing. We propose that regular splashes are controlled by the azimuthal perturbations imposed by the target cross-sectional geometry and that irregular splashes are governed by the fastest-growing unstable Plateau-Rayleigh mode.

DOI: 10.1103/PhysRevE.85.026319 PACS number(s): 47.55.D−, 47.20.Ma, 47.55.nd

I. INTRODUCTION

The impact of liquid drops is a rich phenomenon that continues to draw copious research attention since drop impacts are ubiquitous to many processes in both nature and industry [1–7]. Ink-jet printing, pesticide deposition, and fuel combustion are just a few examples where the effective application of a fluid onto a surface relies on the impact and subsequent splash of drops. Despite the fascination with splashing patterns [8,9], the dominant mechanism that leads to the rim breakup, filament formation, and secondary droplets remains controversial [10–12].

Recently, a better understanding of how to influence splashing (i.e., either enhance or suppress the occurrence of a splash) has been obtained. Drop impacts under different carefully chosen experimental conditions, such as on compliant surfaces [13], on moving surfaces [14], on wetted patterned surfaces [15], in environments of varying pressure and gas composition [16], and with non-Newtonian liquids [6] have provided techniques that can precisely control splashing. The dominant mechanism, however, still remains unclear. One reason for the ambiguity is that for all of the above cases the length scale of the target surface is much larger than the impacting drop diameter. Under such conditions, the impact process is defined by the competition of inertial, viscous, and capillary forces [17,18]. Unfortunately, it is difficult to distinguish the role played by each force, and as a result it has been challenging to formulate reliable theoretical and numerical methods.

In this paper we provide insight into the instability governing the breakup of liquid lamella sheets that develop after drop impact. Liquid drops of diameter D_0 fall onto a target post of equal diameter with impacting speed U_0. A finite amplitude azimuthal perturbation is produced by varying the target cross-sectional geometry, which includes a cylinder and regular polygon shapes. Figure 1 shows the side view of an example drop impact with a cylindrical post with a time interval between frames in terms of the characteristic impact time $\tau^* = D_0/U_0$. Despite the advantage of this simple setup, only a limited number of investigations have focused on drop impacts with obstacles of similar length scales as a window to understanding the complexities of drop splashing [19–25].

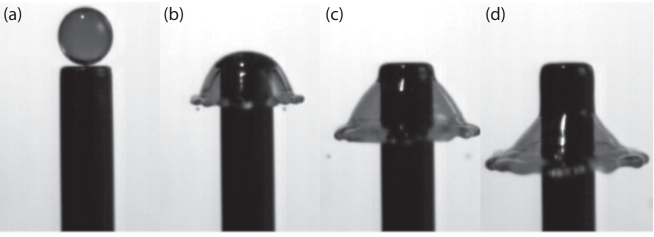

FIG. 1. Side view of a liquid drop composed of water and glycerol impacting a cylindrical post recorded at 40 000 fps. (a) A drop of diameter 2.85 mm with impact velocity of 1.56 m s^{-1} makes contact with the target. The drop deforms and (b) spreads radially to form (c) a liquid lamella sheet. (d) As the sheet expands, undulations along the rim emerge followed by the formation of filaments and secondary smaller droplets. The time interval between frames is equal to the characteristic impact time $\tau^* \approx 1.8$ ms. See Supplemental Material for movie [26].

II. EXPERIMENTAL METHODS

Droplets are created as liquid is injected into a capillary tube using a low-noise syringe pump. The liquid slowly drips out of the tube to form reproducible pendant drops with an average diameter D_0 of 2.85 mm. The liquid is composed of deionized water and glycerol. Food coloring is added to the solution for image enhancement purposes. The liquid has a viscosity of 10 cP and a surface tension with ambient air of 35.3×10^{-3} N m^{-1}. Drops fall from a height of 15 cm before striking the target, hitting the surface with a measured impact velocity U_0 of 1.56 m s^{-1}. All experiments are performed at ambient pressure (101 kPa). The dynamics are described by two dimensionless parameters: the Reynolds number (Re), defined as $\rho D_0 U_0/\mu$, and the Weber number (We), defined as $\rho D_0 U_0^2/\gamma$. Here ρ is the fluid density, U_0 is the impact velocity, D_0 is the drop diameter, μ is the dynamic

---

[*] parratia@seas.upenn.edu

viscosity, and γ is the surface tension. For the given set of experimental parameters, this results in a Re of 550 (i.e., inertial forces dominate viscous forces) and a We of 250 (i.e., inertial forces dominate surface forces). The capillary number, defined as $\mu U_0/\gamma$, is 0.45 meaning that surface forces dominate over viscous forces. Top and side view images are recorded using high-speed photography ranging from 30 000 to 40 000 frames per second.

The target posts are machined out of polyoxymethylene with no surface treatments. The target cross-sectional geometry is varied and includes a cylinder and regular polygon shapes that range from a triangle ($n = 3$) to a decagon ($n = 10$), where n is the number of vertices. The diameter of the cylindrical post is 2.85 mm, equal to the impacting drop diameter, and the impacting cross-sectional surface area is kept constant for all shapes (cylinder and polygons) at 6.38 mm^2. This geometric constraint allows the polygonal circumradius, the radius of a circle that passes through all of the polygon vertices, to be expressed in terms of the initial drop diameter as a function of the number of vertices given by

$$\mathcal{R}(n) = D_0\sqrt{\frac{\pi}{2n\sin(2\pi/n)}}. \tag{1}$$

More importantly, the relevant azimuthal length scale, which is the edge length between vertices, is given by

$$s(n) = 2\mathcal{R}(n)\sin(\pi/n). \tag{2}$$

From Eq. (2), we note that the edge length is largest for $n = 3$ and decreases as the number of vertices increase. This effectively decreases the amplitude of the azimuthal perturbation.

III. RESULTS

A. Effect of target cross section on drop impacts

Figure 2 shows snapshots from the top view of a drop impacting target posts of different cross-sectional geometries. Under similar impacting conditions (i.e., constant Reynolds and Weber numbers) we observe that the spreading and retraction of the liquid lamella is significantly affected by the target cross-sectional geometry. For example, both regular ($3 \leqslant n < 8$) and irregular (cylinder and $n \geqslant 8$) splashing is observed for impacts on polygonal posts. We refer to regular splashing as whenever the number of filaments is equal to the number of target vertices and their location is rotated azimuthally by an angle of π/n with respect to the target orientation. Irregular splashing occurs when the number of filaments that form, and their location, are independent of the target geometry, or number of vertices.

For the cylindrical case, the drop deforms and spreads radially upon impact (Figs. 1 and 2). A thick rim forms at the edge of the lamella sheet due to the accumulation of ejected fluid. As the rim decelerates due to surface tension it becomes susceptible to infinitesimal perturbations that lead to the breakup of the lamella sheet into filaments and secondary droplets. As the cross-sectional geometry of the post is changed, the dynamics of the resulting lamella is significantly altered. Figure 2 (top row) shows example snapshots of geometric lamella for $n = 3$, 4, and 5 at a time $2\tau^*$ after impact, where τ^* is the characteristic impact time. Strikingly, the resulting splash resembles the shape of the polygonal target with an azimuthal rotation of approximately π/n with respect to the target orientation, where n is the number of vertices. For example, a drop that impacts a triangular post results in a triangular-like splash that is shifted by $\pi/3$ with respect to the post (Fig. 2, $n = 3$). For $n \geqslant 8$, the splashing dynamics are similar to the cylindrical post case.

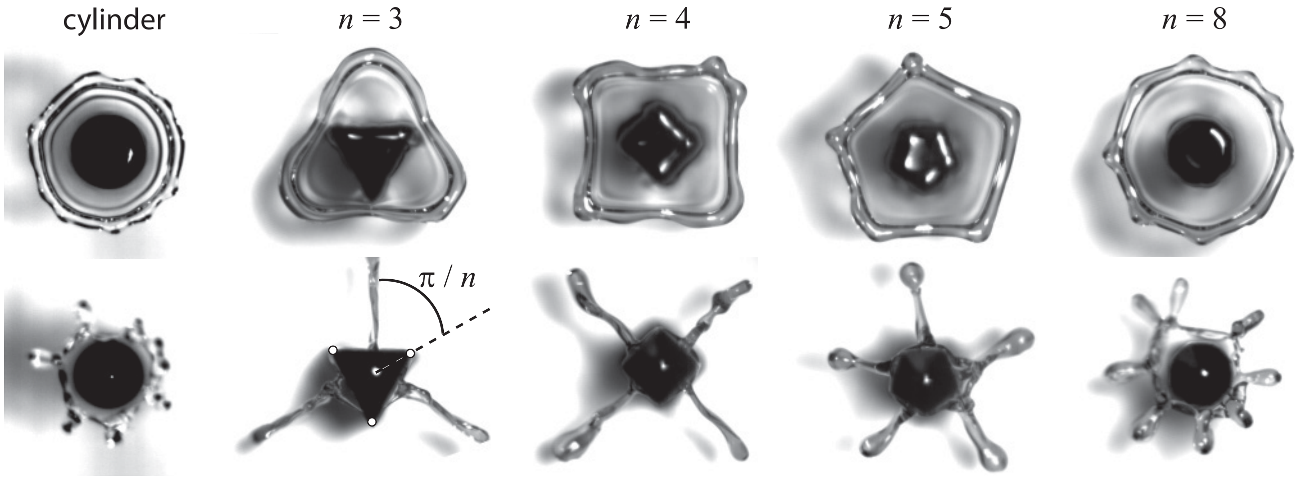

FIG. 2. Top view of liquid drops composed of water and glycerol impacting geometric target posts with a Re of 550 and a We of 250. (Top row) Geometrically-shaped lamella $2\tau^*$ after impact, where τ^* is the characteristic impact time D_0/U_0, with a cylindrical, triangular ($n = 3$), square ($n = 4$), pentagon ($n = 5$), and octagon ($n = 8$) post. For $n < 8$, the resulting lamella shapes are identical to the target geometry but are rotated by π/n due to the azimuthal variation of viscous dissipation. (Bottom row) Filament formation $4\tau^*$ after impact shows that the splashing dynamics depend on the target cross-sectional geometry. The lamella rims for $n = 3$, 4, and 5 breakup in a controlled manner and form the exact number of filaments as the number of target vertices. The lamella rims for the cylinder post and $n \geqslant 8$ targets, however, breakup in a similar fashion independent of target shape. See Supplemental Material for movies [26].

B. Dynamics of geometrically shaped lamella

The dynamics of lamella sheets are characterized by measuring the normalized splash diameter β, which is the ratio of the instantaneous splash diameter $D(\tau)$ and the initial drop diameter D_0, as a function of normalized time $\tau = t/\tau^*$ [Fig. 3(a)]. Here $\tau = 0$ is taken to be the instant that the drop makes contact with the surface of the target. The first few instants, as the lamella spreads along the target surface from the point of impact, are not able to be resolved and represent the initial flat part of $\beta(\tau)$. Each plot of $\beta(\tau)$ represents an average of at least five impact events. The maximum normalized splash diameter β_m for all target cross sections is 3.74 ± 0.33. The average value of the maximum normalized splash diameter agrees reasonably well with the scaling laws of $\beta_m \sim \mathrm{Re}^{1/5}$ and with $\beta_m \sim \mathrm{We}^{1/4}$ [27]. This means that inertia, viscous, and surface forces play important roles in the splashing dynamics despite the minimal interaction between the drop and the target surface. This is in accordance with an impact number $P \equiv \mathrm{We}/\mathrm{Re}^{4/5}$ close to unity [27]. Values of $P < 1$ describe impacts for inviscid fluids and $P > 1$ describe impacts of viscous fluids. For this study, the impact number is $P \approx 1.6$ and therefore follows closely with both scaling laws.

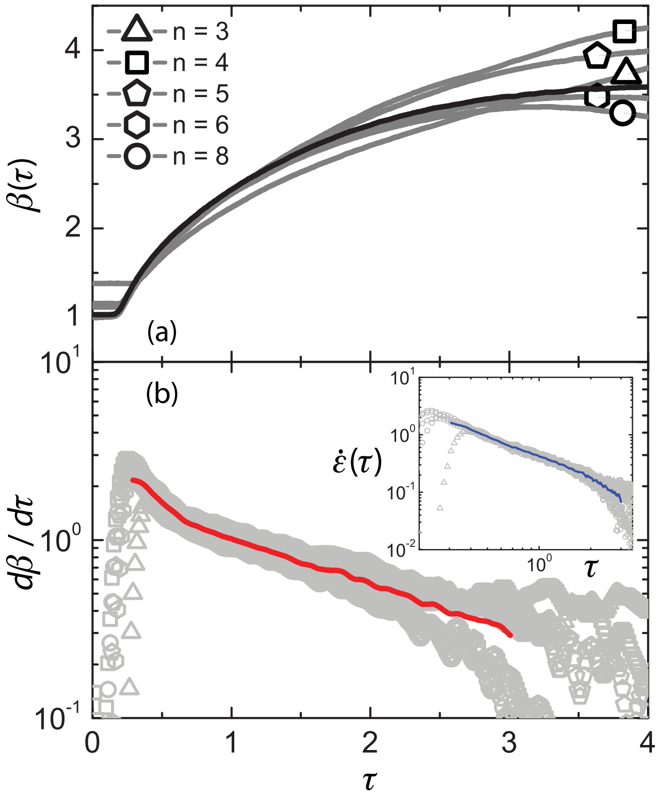

FIG. 3. (Color online) (a) The lamella splash diameter normalized by the initial drop diameter plotted as a function of normalized time τ. The average maximum splash diameter for all targets is 3.74 which agrees well with both scaling laws of $\beta_m \sim \mathrm{Re}^{1/5}$ and $\beta_m \sim \mathrm{We}^{1/4}$. (b) The velocity of the expanding splash diameter exhibits two exponentially decaying regimes. At early times ($0.3 < \tau < 0.7$) a fast decay is due to the inertia dominated deformation of the drop as it contacts the target. At later times ($0.7 < \tau < 3$) a second slower decay is due to viscous dissipation and surface forces impeding lamella expansion. (Inset) The average strain rate on the expanding lamella sheet $\dot{\varepsilon} = \dot{\beta}/\beta$ shows two exponential regimes.

The liquid lamella expansion rate, computed from the splash diameter $d\beta/d\tau$, shows two exponentially decaying regimes [Fig. 3(b)]. At early times ($0.3 < \tau < 0.7$), the rim expansion follows a fast decay due to the inertia dominated deformation of the drop as it comes into contact with the target. The initial downward momentum is transferred horizontally, producing radial expansion parallel to the surface of the target. At later times ($0.7 < \tau < 3$), the rim expansion is described by a second slower decay than the first regime. Viscous dissipation is present due to shear flow at the target surface as well as surface forces due to the increase in surface area, both working to impede the lamella expansion. For $\tau < 0.3$, the rapid increase in the expansion rate is due to an artifact as the initial transient of spreading along the target surface is not captured until the lamellae expand beyond the target circumradius. The corresponding lamella strain rate $\dot{\varepsilon}$, computed here as the ratio of the expansion rate $d\beta/d\tau$ and the normalized splash diameter $\beta(\tau)$, shows two exponential regimes in accordance with biaxial extensional flow. This would suggest that the splashing dynamics could be very different for non-Newtonian fluids where the extensional viscosity can vary by orders of magnitude under strong extensional flows [6,20].

As noted earlier, the resulting splash resembles the target polygonal shape but with an azimuthal rotation with respect to the target orientation (e.g., Fig. 2, $n = 3$). The rotation of the lamella by π/n relative to the target can result from two possible mechanisms: (i) the rapid decrease in kinetic energy as the drop deforms after impact and (ii) the azimuthal dependence of viscous dissipation in the boundary layer that is formed in the vicinity of the target surface. Let us consider a geometric cross-sectional target that is described by the smallest and the largest radial distance from the origin, the apogee r, and the circumradius $\mathcal{R}$, respectively. For a liquid drop that expands radially in contact with the surface from the origin, the time it takes for the liquid lamella to reach the apogee is less than the time it takes to reach the circumradius. The fluid at the apogee experiences less of a decrease in kinetic energy and less viscous dissipation than the fluid at the circumradius. Hence the fluid velocity is larger at the apogee than at the circumradius resulting in a geometrical lamella that are shifted by π/n with respect to the target vertices, for $n < 8$.

C. Rim instability: Regular and irregular splashing

Once the maximum splash diameter is reached, the liquid lamella retracts inward. Finger formation and secondary droplets result as the outer rim breaks up to minimize the increase in surface energy. We observe that for polygonal targets, the ability to create geometric lamellae that undergo controlled breakup into n filaments depends on the target cross-sectional geometry and holds for targets with $n < 8$ only (Fig. 2, bottom row). Specifically, there is a transition in the splashing stability from regular ($3 \leqslant n < 8$) to irregular ($n \geqslant 8$) breakup of the liquid lamellae. We propose that there is a competition between the finite amplitude perturbation imposed from the target cross-sectional geometry and the most unstable mode determined by the dominant instability, which in this case is similar to the Plateau-Rayleigh (PR)

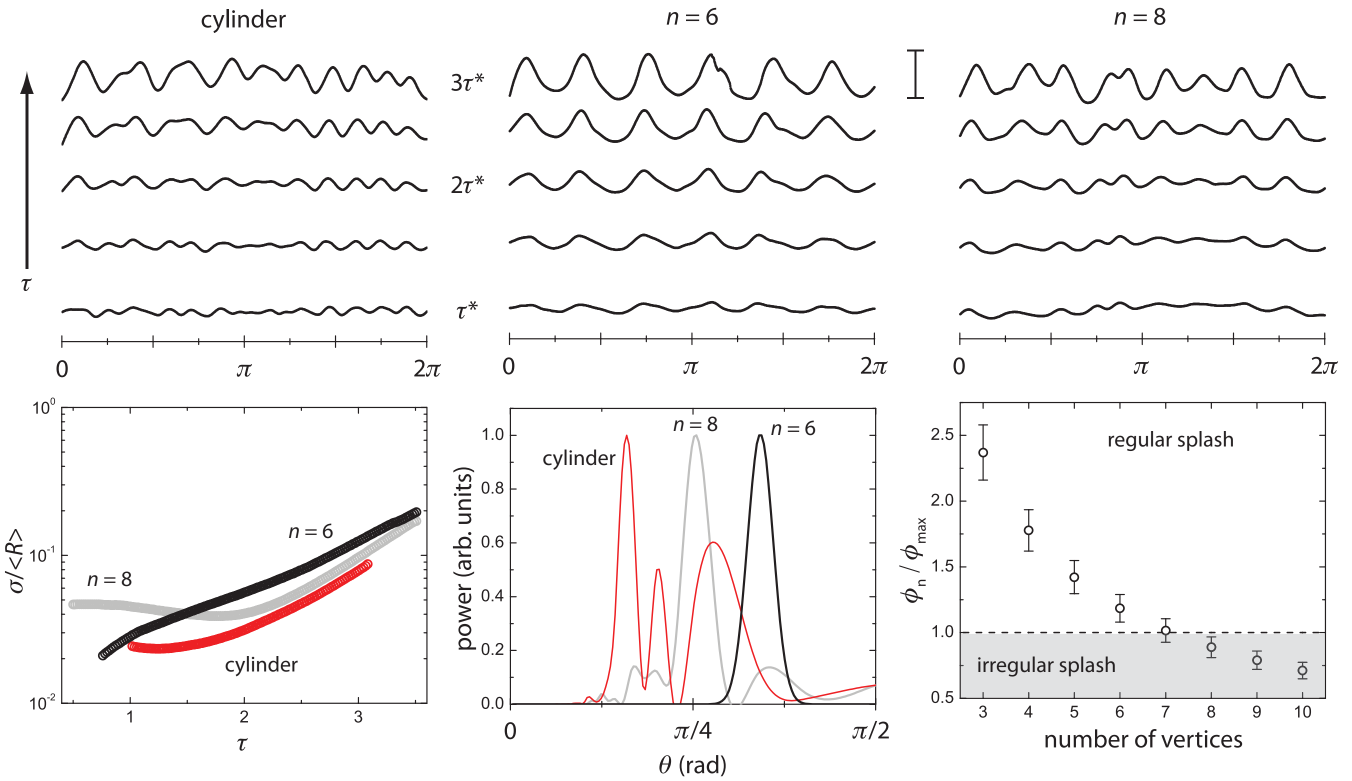

FIG. 4. (Color online) (Top row) Evolution of the radial profile for expanding lamella sheets for the time interval $\tau^* < \tau < 3\tau^*$ after drop impact on a cylinder, hexagon ($n = 6$), and octagon ($n = 8$) targets. Six equidistant peaks are evident over the entire interval for the hexagon case. The peaks for the cylinder and octagon case are not evenly spaced and the number decreases due to merging. Scale bar represents 1.75 mm. (Bottom row) *Left:* The deviations in the undulation amplitude σ normalized by the average lamella radius $\langle R\rangle$ increases exponentially with time. *Middle:* The periodograms of the radial profiles of the lamella sheets for the three cases at $2\tau^*$ after impact. There is a single narrow peak at $\pi/3$ for the $n = 6$ case and a broad distribution of values with multiple peaks for the cylinder and $n = 8$ cases. *Right:* A comparison of the target perturbation amplitude ϕ_n and the most unstable azimuthal mode $\phi_{\max}$ of a toroid jet determined by the Plateau-Rayleigh instability. Regular splashing occurs when $\phi_n/\phi_{\max} > 1$ for targets with $3 \leqslant n < 8$ and irregular splashing occurs when $\phi_n/\phi_{\max} < 1$ for targets with $n \geqslant 8$.

instability [12,19,28]. Other possible mechanisms that have been proposed include the Richtmyer-Meshkov [29] and the Rayleigh-Taylor [9,10,25,30] instabilities.

To gain insight into the mechanism responsible for the breakup and retraction of the lamella, an analysis of the corrugations around the expanding rim was performed. The top row of Fig. 4 shows the evolution of the azimuthal profile of lamella sheets after drop impact on a cylinder (left), hexagon (center), and octagon (right) target over the time interval of τ^* to $3\tau^*$. At early times ($\tau = \tau^*$), the amplitude of rim undulations is similar for all three cases. At later times, however ($\tau^* < \tau \leqslant 3\tau^*$), it is evident that the radial profile for the hexagon case is different than the profiles for the cylinder and octagon cases. The typical behavior of lamella sheets for impacts on targets with $3 \leqslant n < 8$ is that there are n equidistant peaks apparent over the entire splash process, similar to the six equidistant peaks for the hexagon case. For other targets ($n \geqslant 8$) the peaks are unevenly distributed and the number decreases as filaments merge during the sheet expansion, similar to the profiles for the cylinder and octagon cases (Fig. 4, top row).

For all cases ($3 \leqslant n \leqslant 10$ and cylinder), the amplitude of rim undulations increase with time. The fluctuations of the corrugations, which are quantified by the ratio of the standard deviation σ about the average lamella sheet radius $\langle R\rangle$, grow exponentially with time (Fig. 4, bottom left). The rates of growth, evident by the slope of the straight portion of the curves for $\tau > 2$, are similar for all cases independent of the target cross-sectional geometry. This is not surprising because the mechanism behind every lamellae breakup, whether it undergoes regular or irregular splashing, is driven by surface tension. The exponential growth rate, however, is indicative of a PR instability. The dispersion relation associated with the most unstable mode of the PR instability is given by $\omega_{\mathrm{PR}} = 0.34\sqrt{\gamma/\rho a^3}$, where γ is the surface tension, ρ is the fluid density, and a is the radius of the fluid jet [31]. For the current experimental parameters, the time scale of the PR instability would be approximately 2.7 ms. The average characteristic time scale of growth in fluctuations of expanding lamellae, extracted by fitting an exponential function to the curve for $\tau > 2$, is measured to be 2.1 ± 0.4 ms, in good agreement with the PR time scale.

For further comparison, we compute the periodograms of the radial profiles for the three cases (cylinder, $n = 6$, and $n = 8$) at $2\tau^*$ (Fig. 4, bottom middle). The periodogram of the radial profile for the hexagon case is a single narrow peak centered about $\pi/3$. It is typical for the periodograms to contain a single peak centered about π/n for targets with $3 \leqslant n < 8$ vertices.

The periodograms for other targets (cylinder and $n \geqslant 8$), however, are broad and contain multiple peaks, represented in the periodograms for the cylinder and octagon cases. This supports the idea that the perturbation imposed from the target cross-sectional geometry for $3 \leqslant n < 8$ overwhelms the most unstable mode and is therefore a determining factor in the evolution of the lamella. The cylinder and octagon cases, however, contain a distribution of values as the imposed target perturbation is small compared to the most unstable mode, making the rims unstable and susceptible to infinitesimal perturbations.

It seems reasonable to conclude that a regular splash will occur when the azimuthal perturbation imposed by the target cross-sectional geometry is larger than the most unstable mode of the expanding toroidal jet, experimentally equivalent to the thick outer rim. The thin liquid lamella sheet that connects the outer rim to the target post is neglected since we believe that it does not contribute to the rim instability. This simplification is supported by our observations that, for moderate Re, there are no ripples in the lamella sheet (Fig. 2) as seen for high Re impacts of $\mathcal{O}(10^4)$ [19]. Furthermore, the lamellae are seen to break from the outermost points of the rim rather than from within the sheet connecting the target to the rim.

Utilizing the observations that the fluctuations in the rim corrugations increase exponentially with a characteristic time similar to that associated with the PR dispersion relation ω_{PR}, we approximate the most unstable mode of a toroidal jet as determined by the PR instability and compare it to the azimuthal perturbation imposed due to the target geometry. The rim volume can be expressed as a fraction of the initial drop volume $V_r = \varepsilon V_0$, with $0 < \varepsilon < 1$. Denoting a as the minor radius of the toroid, R_m as the major radius of the toroid, and R_0 as the initial radius of the impacting drop, the rim volume is given by

$$2\pi^2 a^2 R_m = \frac{4}{3}\pi \varepsilon R_0^3. \qquad (3)$$

At maximum expansion the torus minor radius can be written in terms of the maximum splash radius R_m and the normalized splash radius β_m and is given by

$$a = R_m \sqrt{\frac{2\varepsilon}{3\pi\beta_m^3}}. \qquad (4)$$

Using the scaling relations for β_m [27] and an average measured value for ε of 0.65 [19,21], Eq. (4) predicts the minor radius a to be 0.27 mm. This value agrees well with observations of the rim thickness for geometric lamella, measured to be $a = 0.3$ mm.

Analogous to the most unstable wavelength of a cylindrical jet [32], the most unstable azimuthal mode for a toroid jet determined by the PR instability [33,34] is given by

$$\phi_{\max} = \frac{\lambda_{\max}}{R_m} = \frac{9.02\, a}{R_m} = 9.02\sqrt{\frac{2\varepsilon}{3\pi\beta_m^3}}. \qquad (5)$$

The amplitude of the azimuthal perturbation imposed for regular polygon targets is taken to be

$$\phi_n = \pi/n. \qquad (6)$$

The ratio of the target perturbation ϕ_n and the most unstable azimuthal mode of a toroid jet $\phi_{\max}$ is plotted as a function of target vertices n (Fig. 4, bottom right). Interestingly, we see that for targets with $3 \leqslant n < 8$ vertices, the azimuthal perturbation imposed by the target geometry is larger than the most unstable azimuthal PR mode, or that $\phi_n/\phi_{\max} > 1$. These conditions will produce a regular splash, in agreement with observations (Fig. 2). For targets with $n \geqslant 8$, however, the azimuthal perturbation is smaller than the most unstable PR mode, $\phi_n/\phi_{\max} < 1$, suggesting that the lamella rim is susceptible to infinitesimal perturbations and will produce an irregular splash, independent of target geometry. We note that R_m does not explicitly appear in Eq. (5) as we assume that the maximum radius for the toroid jet is similar to circumradius of a geometrically shaped lamella, a reasonable assumption from Fig. 3(a). Finally, to show that these results are independent of scaling arguments, both $\beta_m \sim \mathrm{We}^{1/4}$ and $\beta_m \sim \mathrm{Re}^{1/5}$ are used in place of the normalized splash radius in Eq. (5), and the upper and lower bounds are shown with error bars.

IV. CONCLUSION

We have shown that the expansion and subsequent breakup of the outer rim of liquid lamellae can be controlled by length scales on the order of the impacting drop diameter. Under identical impact conditions of constant Reynolds and Weber numbers, we observe unique splashing dynamics by simply varying the target cross-sectional geometry to include a cylinder and regular polygon shapes. For polygon targets with $3 \leqslant n < 8$ vertices, the expanding lamellae resemble the geometric cross-section of the target, but are rotated by an angle of π/n with respect to the target orientation. We find that the breakup of the outer rim and liquid lamellae are well controlled and reproducible. The number of filaments that form during splashing is equal to the number of vertices n of the target. For other targets (cylinder and $n \geqslant 8$), the expansion and breakup of the outer rim and liquid lamellae are independent of the target geometry.

We find that there are two distinct splashing regimes depending on the number of target vertices: regular splashing ($3 \leqslant n < 8$) and irregular splashing (cylinder and $n \geqslant 8$). We propose that the transition in splashing stability is a result of the competition between the amplitude of the azimuthal perturbation imposed by the target cross-sectional geometry and the most unstable azimuthal mode, determined by the Plateau-Rayleigh instability, of the expanding outer rim. For $3 \leqslant n < 8$ polygon targets, regular splashing occurs since the imposed target perturbation is large enough to overwhelm the most unstable mode and effectively control the dynamics of the splash. For the cylinder and $n \geqslant 8$ targets, irregular splashing occurs since the imposed target perturbation is smaller than the most unstable mode and the resulting splash dynamics are independent of the target geometry. The rim dynamics are instead governed by the most unstable azimuthal Plateau-Rayleigh mode.

In summary, we show that drop splashing can be potentially controlled by geometric features of the target. The experiments presented here provide a new method that systematically probes the effects of azimuthal perturbations on the expanding lamellae after drop impact. While our experimental observations indicate that the splashing phenomenon is dominated by the Plateau-Rayleigh instability, questions still remain. One important parameter to investigate further is the dependence of the ratio of the maximum splash radius to the minor radius of the outer rim, expressed in Eq. (4), on varying impact conditions (i.e., changing both the Re and the We). This would provide a better understanding on the limiting case for irregular splashing of liquid lamellae.

ACKNOWLEDGMENTS

We thank D. Hu, D. Lohse, N. C. Keim, V. Garbin, X. N. Shen, and M. Garcia for helpful discussions. We also thank P. Rocket for fabricating the regular n-sided polygon target posts. This work was partially supported by the National Science Foundation through the award CBET-0932449.

---

[1] A. M. Worthington, *A Study of Splashes* (Longman, Green, and Co., London, 1908).
[2] H. E. Edgerton and J. R. Killian, *Moments of Vision: The Stroboscopic Revolution in Photography* (MIT Press, Cambridge, MA, 1979).
[3] D. H. Peregrine, J. Fluid Mech. **106**, 59 (1981).
[4] P. G. de Gennes, Rev. Mod. Phys. **57**, 827 (1985).
[5] A. Prosperetti and H. N. Oguz, Annu. Rev. Fluid Mech. **25**, 577 (1993).
[6] V. Bergeron, D. Bonn, J. Y. Martin, and L. Vovelle, Nature (London) **405**, 772 (2000).
[7] V. Bergeron and D. Quéré, Phys. World **14**, 27 (2001).
[8] H. Marmanis and S. T. Thoroddsen, Phys. Fluids **8**, 1344 (1996).
[9] S. T. Thoroddsen and J. Sakakibara, Phys. Fluids **10**, 1359 (1998).
[10] R. F. Allen, J. Colloid Interface Sci. **51**, 350 (1975).
[11] A. L. Yarin and D. A. Weiss, J. Fluid Mech. **283**, 141 (1995).
[12] L. V. Zhang, P. Brunet, J. Eggers, and R. D. Deegan, Phys. Fluids **22**, 122105 (2010).
[13] R. E. Pepper, L. Courbin, and H. A. Stone, Phys. Fluids **20**, 082103 (2008).
[14] J. C. Bird, S. S. H. Tsai, and H. A. Stone, New J. Phys. **11**, 063017 (2009).
[15] M. Lee, Y. S. Chang, and H.-Y. Kim, Phys. Fluids **22**, 072101 (2010).
[16] L. Xu, W. W. Zhang, and S. R. Nagel, Phys. Rev. Lett. **94**, 184505 (2005).
[17] M. Rein, Fluid Dyn. Res. **12**, 61 (1993).
[18] A. L. Yarin, Annu. Rev. Fluid Mech. **38**, 159 (2006).
[19] A. Rozhkov, B. Prunet-Foch, and M. Vignes-Adler, Phys. Fluids **14**, 3485 (2002).
[20] A. Rozhkov, B. Prunet-Foch, and M. Vignes-Adler, Phys. Fluids **15**, 2006 (2003).
[21] A. Rozhkov, B. Prunet-Foch, and M. Vignes-Adler, Proc. R. Soc. London A **460**, 2681 (2004).
[22] C. Josserand, L. Lemoyne, R. Troeger, and S. Zaleski, J. Fluid Mech. **524**, 47 (2005).
[23] S. Bakshi, I. V. Roisman, and C. Tropea, Phys. Fluids **19**, 032102 (2007).
[24] H. J. Subramani, T. Al-Housseiny, A. U. Chen, M. F. Li, and O. A. Basaran, Ind. Eng. Chem. Res. **46**, 6105 (2007).
[25] E. Villermaux and B. Bossa, J. Fluid Mech. **668**, 412 (2011).
[26] See Supplemental Material at http://link.aps.org/supplemental/10.1103/PhysRevE.85.026319 for movies.
[27] C. Clanet, C. Beguin, D. Richard, and D. Quere, J. Fluid Mech. **517**, 199 (2004).
[28] J. Eggers, Rev. Mod. Phys. **69**, 865 (1997).
[29] D. Gueyffier and S. Zaleski, C.R. Acad. Sci., Ser. IIc: Chim **326**, 839 (1998).
[30] R. Krechetnikov and G. M. Homsy, J. Colloid Interface Sci. **331**, 555 (2009).
[31] H. Lhuissier and E. Villermaux, Phys. Fluids **23**, 091705 (2011).
[32] L. Rayleigh, Proc. London Math. Soc. **4**, 10 (1878).
[33] E. Pairam and A. Fernández-Nieves, Phys. Rev. Lett. **102**, 234501 (2009).
[34] J. D. McGraw *et al.*, Soft Matter **6**, 1258 (2010).